Electronic Supplementary Information

Promotion of Oxygen Reduction Reaction on a Double Perovskite Electrode by a Water-induced Surface Modification

Jun Hyuk Kim[a, d], Seonyoung Yoo[a], Ryan Murphy[a], Yu Chen[a], Yong Ding[a], Kai Pei[a], Bote Zhao[a], Guntae Kim[c*], YongMan Choi[b*] and Meilin Liu[a*]

[a] School of Materials Science and Engineering, Georgia Institute of Technology, Atlanta, Georgia 30332, USA

[b] College of Photonics, National Chiao Tung University, Tainan 71150, Taiwan

[c] Department of Energy Engineering, Ulsan National Institute of Science and Technology (UNIST), Ulsan, 689–798, Republic of Korea

[d] Current address: Department of Materials Science and Engineering, Korea Advanced Institute of Science and Technology, 291 Daehak-ro, Yuseong-gu, Daejeon, 34141, Republic of Korea

E-mail: gtkim@unist.ac.kr; ymchoi@nctu.edu.tw; meilin.liu@mse.gatech.edu

Experimental details

Material synthesis and physical characterization

PBCC powders were synthesized using the citric-combustion method. Stoichiometric amounts of $Pr(NO_3)_3 \cdot 6H_2O$, $Ba(NO_3)_2$, $Ca(NO_3)_2 \cdot 4H_2O$, and $Co(NO_3)_2 \cdot 6H_2O$ were dissolved in distilled water with a proper amount of citric acid. An adequate amount of ethylene glycol was added to the solution after the mixture was dissolved. After a viscous resin was formed, the mixture was heated to roughly 250 ^oC in air, which was followed by combustion to form fine powders. These powders were then calcined at 900 ^oC for two hours, with the resulting powders then ball-milled for 24 hours. The calcined PBCC powders were ball-milled again and then sintered at 1125^oC for five hours to achieve a single phase, as confirmed by X-ray diffraction (XRD, PANalytical X-Ray Diffractometer, Alpha-1).

The microstructure and morphology of the PBCC electrode before/after exposure to water were examined using a scanning electron microscope (SEM, LEO-1530). The samples shown in Figure 2, are treated with 3 vol.% H_2O/air at 600^oC for 3 hours. The surface morphology of the PBCC was analyzed with high-resolution transmission electron microscopy (HRTEM) with energy-dispersive X-ray spectroscopy (EDX). It was found that water can decorate PBCC surfaces with BCO NPs.

For a Raman profilometry analysis, the PBCC powders were dry pressed and sintered at 1200^oC for five hours, with a heating/cooling rate of 1.5^oC min^{-1} in an air atmosphere to obtain > 95% relative density.

To demonstrate a controlled size and densities of BCO nano-catalysts, PBCC powder was first dry-pressed in square steel-die and the resulting green bodies were sintered at 1120^oC for 10 hours to form dense pellets. The pellets are then cleaved to reveal the native surface, and subsequently

put in a gas-flowing quartz tube to treat the samples under various temperatures (600~650°C) and pH_2O (1~3 vol.% H_2O). pH_2O was tuned with temperature-controlled water bubbler. The sample are then characterized with SEM (Hitachi S-4800).

X-ray photoelectron spectroscopy (XPS) is conducted by using Sigma Probe (Thermo VG Scientific).

Electrochemical measurements

To determine the area-specific resistance (ASR) of PBCC for oxygen reduction, PBCC electrodes were prepared by tape casting and were then applied to both sides of a $Sm_{0.2}Ce_{0.8}O_{1.9}$ (SDC) electrolyte pellet using a SDC bonding slurry. SDC electrolytes were prepared by uniaxially pressing commercially available SDC powder, followed by sintering at 1450°C for 5 h to achieve a relative density rate of ~98%. PBCC tape was adhered to both sides of the SDC electrolyte using SDC slurry as a bonding layer (3-5 μm). Lastly, the PBCC|SDC|PBCC symmetric cells were fired at 1080°C in air for two hours. Impedance spectra were acquired using a Solartron 1255 HF frequency response analyzer interfaced with an EG&G PAR potentiostat model 273A with an AC amplitude of 10 mV in the frequency range of 100 kHz to 0.01 Hz. Distribution of relaxation time analysis was done with DRT tools, which was obtained from prof. Ciucci's group.[1-3] Electrical conductivity relaxation (ECR) measurements are based on bar pellets using DC 4 probe between 650~750°C.

An anode-supported cell with the Ni-YSZ|ScSZ|SDC|PBCC configuration was prepared to demonstrate the single-cell performance. The Ni-YSZ|ScSZ anode support used here was purchased from Kceracell Co., Ltd. SDC slurry was then drop-coated and subsequently sintered at 1200°C for two hours to form a SDC buffer layer. Thereafter, the cathode of PBCC was applied

onto the SDC buffer layer and fired at 900°C for two hours. The I-V and I-P curves were collected using an in-lab-constructed fuel cell testing station operating within the temperature range of 600~750°C. During the single-cell test, H_2 gas was flowed into the anode side at a flow rate of 50 ml min^{-1}, while the oxidant was fed into the cathode side at a flow rate of 100 ml min^{-1}. To supply wet air, a temperature-controlled bubbler was used.

The cell with the configuration of Ni-$Sm_{0.2}Ce_{0.8}O_{2-\delta}$ (SDC)|SDC|PBCC is devised to demonstrate the superior single cell performance at lower temperatures. NiO, SDC (fuelcellmaterials), and starch was first ball-milled with the weight ratio of 6:4:1 for 24 hours with ethanol as media. Starch was used as fugitive pore former to optimize anode microstructure in this case. The anode composite powder is then dried in 80°C oven to evaporate ethanol. Subsequently, the anode green body was dry-pressed with a square-steel die and fired at 950°C for 1 hours in ambient air. SDC electrolyte was then drop-coated on anode support. SDC electrolyte slurry was made by mixing SDC powders in organic binder which comprised with polyvinylpyrrolidone (PVP), butyl benzyl phthalate, triethanolamine, and terpineol (all from Alfa Aesar). Then the preparation of Ni-SDC|SDC anode-supported half-cell was completed after heat treatment at 1400°C for 5 hours. PBCC cathode is then screen-printed on SDC electrolyte. Ni-SDC cell #1 was initially put on 650°C. Measurements were conducted in a following sequence: dry air→ 1 vol.% H_2O/air→ 3 vol.% H_2O/air (waited for 3 hours) → 10 vol.% H_2O/air→ 20 vol.% H_2O/air→ dry air (return). Ni-SDC cell #2 go through water-mediated surface self-assembly at 565°C. The temperature was chosen as we previously found out that formation of BCO nanoparticles are found when temperature of ~565°C is reached.[4]

Ni-GDC cell are prepared in a similar way as Ni-SDC cells. NiO-GDC10 (NiO:GDC10 = 6:4, fuelcellmaterials) anode powders was dry-pressed with a square-steel die, and GDC20 powders

(fuelcellmaterials) suspended in viscous organic binder was drop coated and sintered at 1450°C for 5 hours. PBCC cathode is then screen-printed on GDC electrolyte.

Proton uptake measurement

The thermogravimetric analysis of the PBCC powder was conducted on a TA Instruments SDT Q600 device. The samples were heated from room temperature to 1000°C at 10°C per minute under an argon flow at 100 SCCM.

In situ Raman Spectroscopy

Raman spectra were obtained using a Renishaw RM 1000 spectromicroscopy system (~2 μm spot size). An air-cooled Ar laser (CVI Melles Griot) emitting at 514 nm was used for the excitation of the Raman signal in this study, operating at a total power of 7 mW. A Harrick environmental chamber was used for the *in situ* Raman tests.[5] An *in situ* time-resolved study was conducted by positioning the laser spot on the same location. To take *in situ* Raman spectroscopic measurements, Ag wires were attached to a PBCC/SDC/PBCC symmetric cell. Synthetic air (N_2 79%, O_2 21%, Airgas) metered with mass flow controllers was introduced into the chamber. To introduce 3 vol.% water into the gas, a room-temperature bubbler was used.

Computational Method

Periodic density functional theory (DFT) calculations were carried out using the Vienna ab initio simulation package (VASP)[6] with the projector-augmented-wave (PAW) method.[7] For optimization of the bulk structure, $PrBa_{0.75}Ca_{0.25}CoO_6$ (PBCC; $Pr_4Ba_3Ca_1Co_8O_{24}$; *P4/mmm*) was used, similarly to previous studies.[8, 9] We utilized the spin-polarization method with generalized

gradient approximation (GGA) using the Perdew-Burke-Ernzerhof (PBE)[10] exchange-correlation functional for PBCC.[11] A kinetic energy cutoff for a plane wave basis set of 415 eV was used. Monkhorst-Pack meshes[12] with the (3 × 3 × 3) and (3 × 3 × 1) were applied for bulk and 2-D surface calculations. For the 2D-surface calculations, slabs were separated by a vacuum space of 15 Å to avoid any interactions between slabs. PBCC(010) was chosen for the surface calculation. The adsorption energy (E_{ad}) of O_2 and H_2O on a surface was calculated by E_{ad} = E[adsorbate-surface] − (E[surface] + E[adsorbate]), where E[adsorbate-surface] and E[surface] are the predicted electronic energies for an adsorbed surface species on a surface and its bare surface, respectively. E[adsorbate] is that for gas-phase triplet O_2 or H_2O. In order to determine the coadsorption effect between surface oxygen and hydroxyl species on PBCC, coadsorption energies were also calculated using E_{coad} = [E(adsorbate-surface) – (E[surface] + n·E[O_2] + m·E[H_2]/2)]/(n + m), where n and m are the number of oxygen and hydroxyl species. Vibrational frequencies were calculated using the VASP using the optimized structures. The reaction barriers were determined by the climbing image-nudged elastic band (CI-NEB)[13] method. In this study, coverage in monolayer (ML) is the number of hydroxyl species/the total active sites of 7 on the defective PBCC surface.

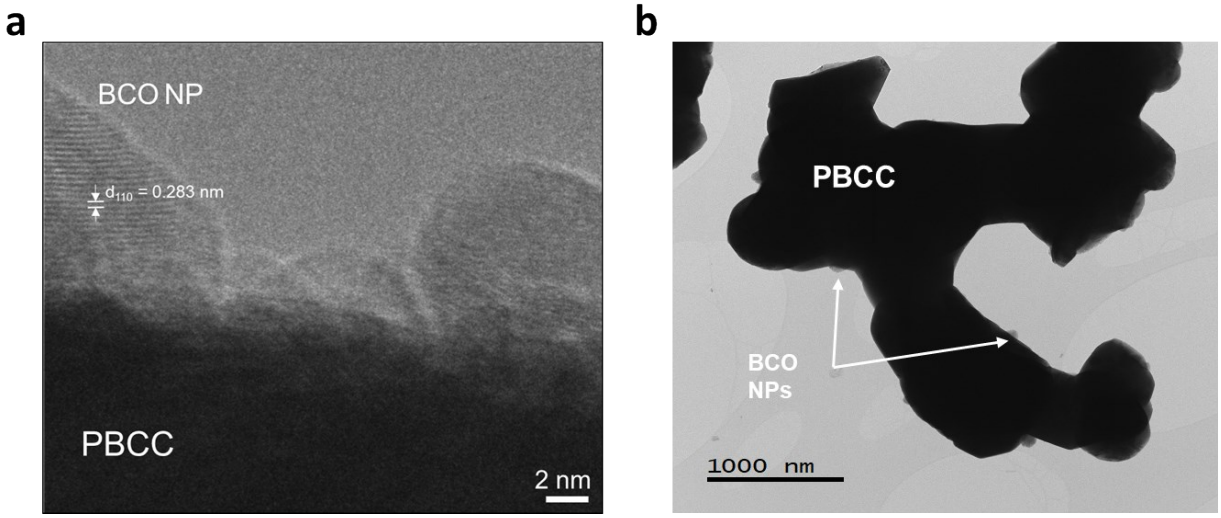

Figure S1. (a) HRTEM image of PBCC, annealed in 3 vol.% H_2O at 600°C for 3 hours (b) TEM image of wet annealed PBCC power with NPs

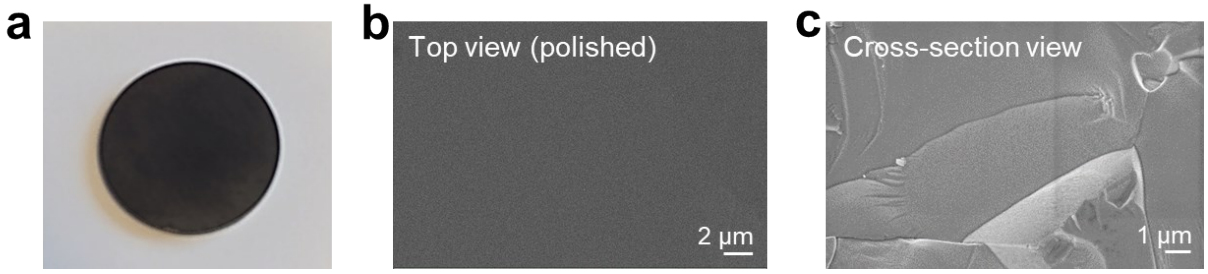

Figure S2. (a) Camera image of dense ceramic pellet of PBCC used for Raman profilometry. SEM images of (b) the Top view and (c) the cross-section view of the PBCC pellet.

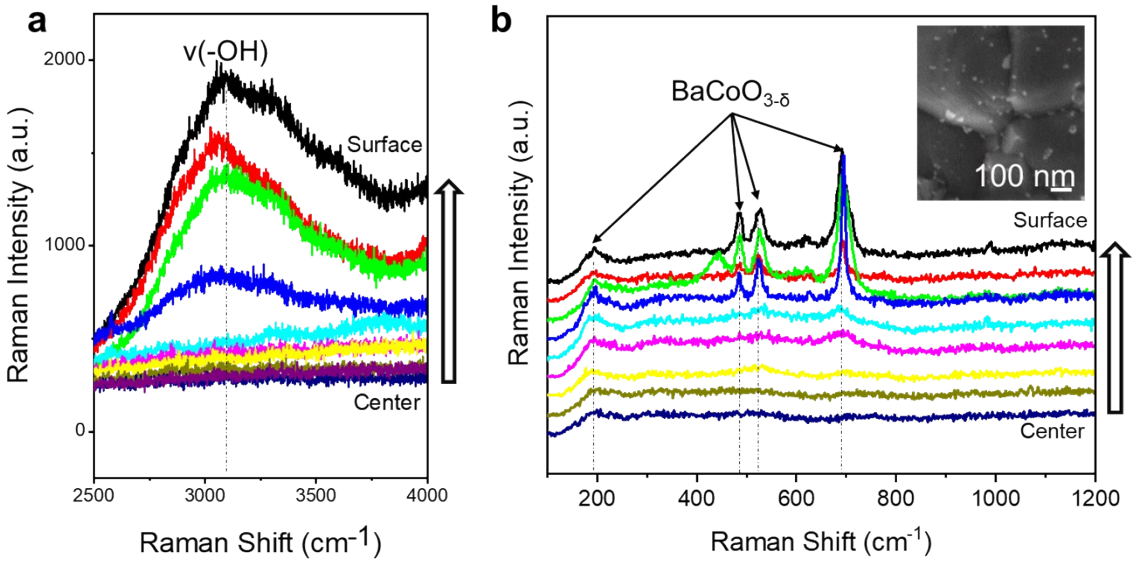

Figure S3. Raman profilometry of wet-annealed PBCC dense pellet scanning from center to surface. (a) Spectrum regime of 2500 cm^{-1} to 4000 cm^{-1}. As scanning toward surface, band of *v*(-OH) gets prominent. (b) Spectrum regime of 100 cm^{-1} to 1200 cm^{-1}. As scanning toward surface, structure of BCO are revealed. (inset) corresponding cross-section SEM image

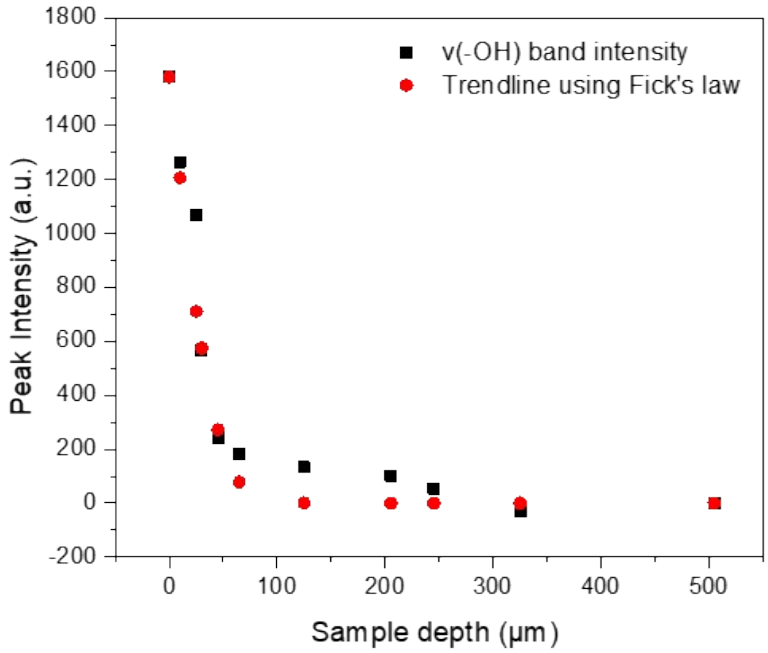

Figure S4. *v*(-OH) Raman band intensity as function of sample depth. The data trend agrees with Fick's law which may support bulk proton diffusion inside PBCC double perovskite structure.

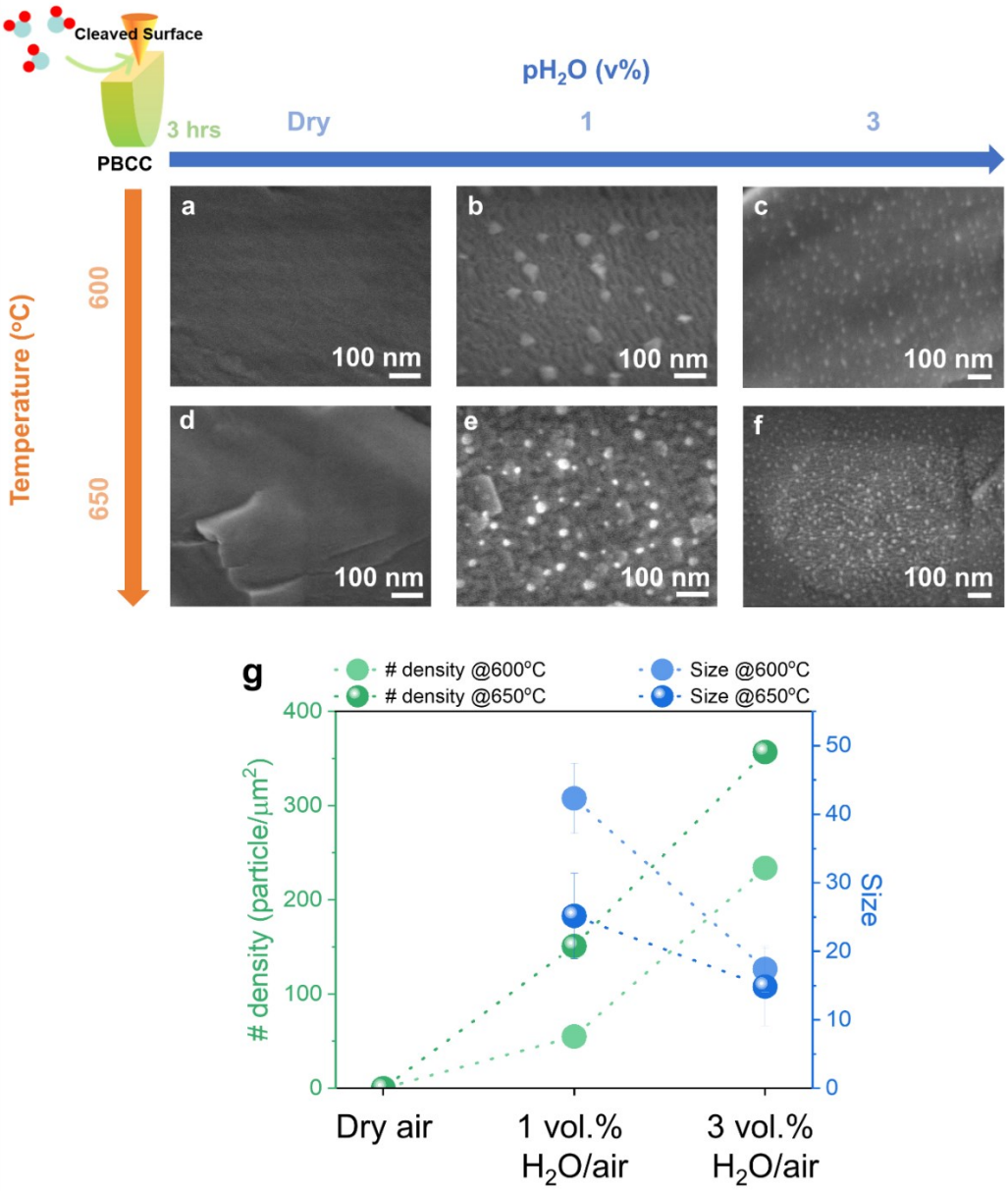

Figure S5. Controlled size and densities of BCO nano-catalysts self-assembled on PBCC cleaved surface at various temperatures and water vapor pressure (pH_2O). (a-f) Scanning electron microscope (SEM) images of PBCC cleaved surface in terms of temperatures and pH_2O. (g) Quantitative analyses of water-mediated self-assembled nanoparticles: number density (# density, particle/μm^2) and size of nanoparticles depending on the temperature and water partial pressure (pH_2O)

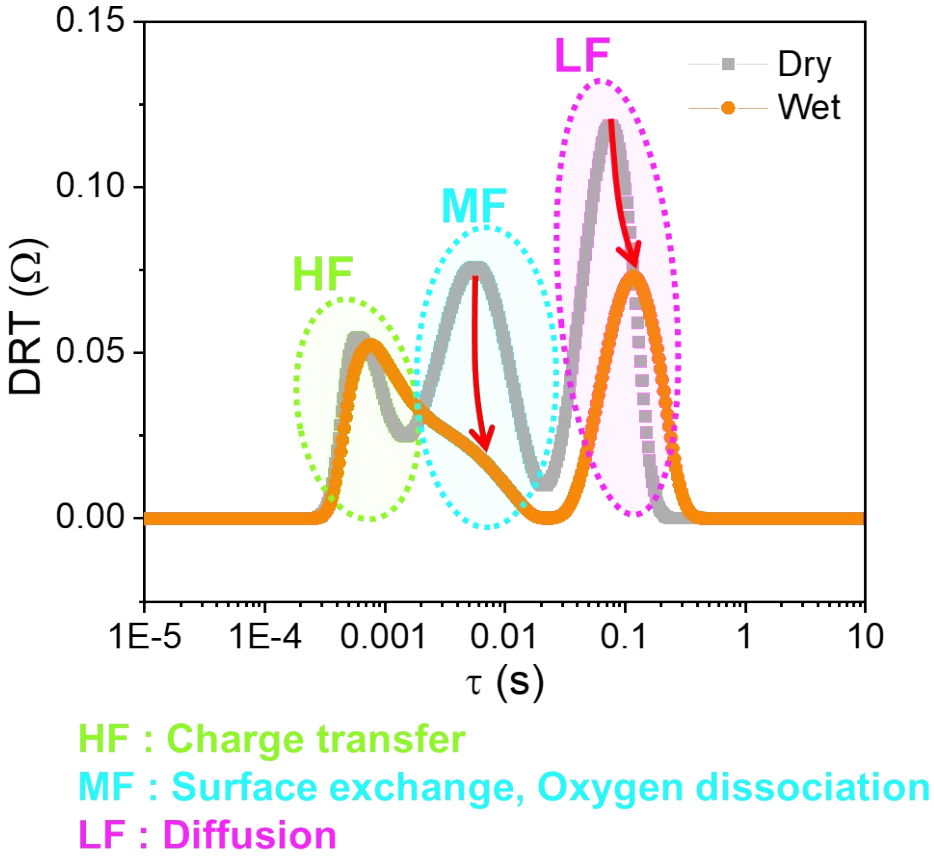

Figure S6. Distribution of relaxation time (DRT) analyses of porous $PrBa_{0.8}Ca_{0.2}Co_2O_{5+\delta}$ in dry (gray color) and wet air (orange color) at 750°C.

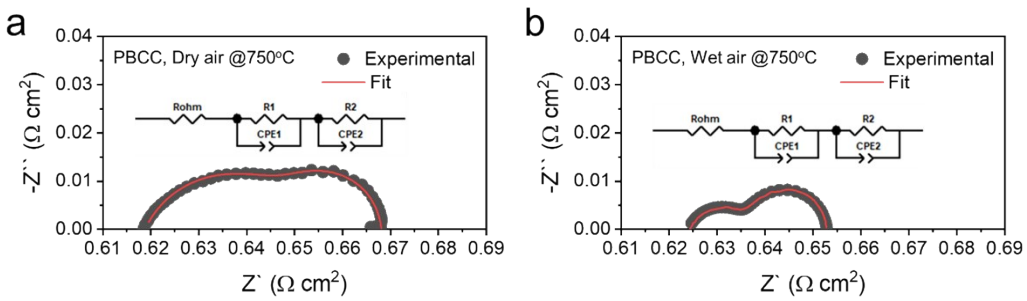

Figure S7. Nyquist plots for the PBCC symmetrical cell and the corresponding fitted impedance spectra using equivalent circuit model with (a) dry and (b) wet air at 750°C.

Table S1. The parameters obtained from the fitting of the equivalent circuits for PBCC electrodes under dry and wet air.

PBCC, Dry				*PBCC, Wet*			
R_1 (Ω cm^2)	C_1 (F cm^{-2})	R_2 (Ω cm^2)	C_2 (F cm^{-2})	R_1 (Ω cm^2)	C_1 (F cm^{-2})	R_2 (Ω cm^2)	C_2 (F cm^{-2})
0.0339	*0.273*	*0.0175*	*8.937*	*0.0131*	*0.255*	*0.0169*	*11.587*

More information can be obtained from the impedance spectra to evaluate the ORR kinetics of PBCC before and after exposure to water vapor. Accordingly, an equivalent circuit model, consisting of resistors (R) and constant phase elements (CPE) with a configuration of R_{ohm}-(R_1-CPE_1)-(R_2-CPE_2), is used to fit the impedance spectra. In this model, R_{ohm} is the ohmic resistance of the electrolyte, R_1 is the resistance to oxygen surface exchange, and R_2 is the resistance to diffusion of oxygen species on cathode surface. The detailed fitting data are listed in Table S1 and presented in Fig. S7. Impedance analysis indicates that R_1 value under wet air is greatly reduced, implying that surface exchange of the electrode is largely improved after water-mediated surface self-assembly of BCO nanoparticles. Similarly, R_2 is reduced as well, indicating enhanced surface diffusion at BCO-PBCC interfaces.

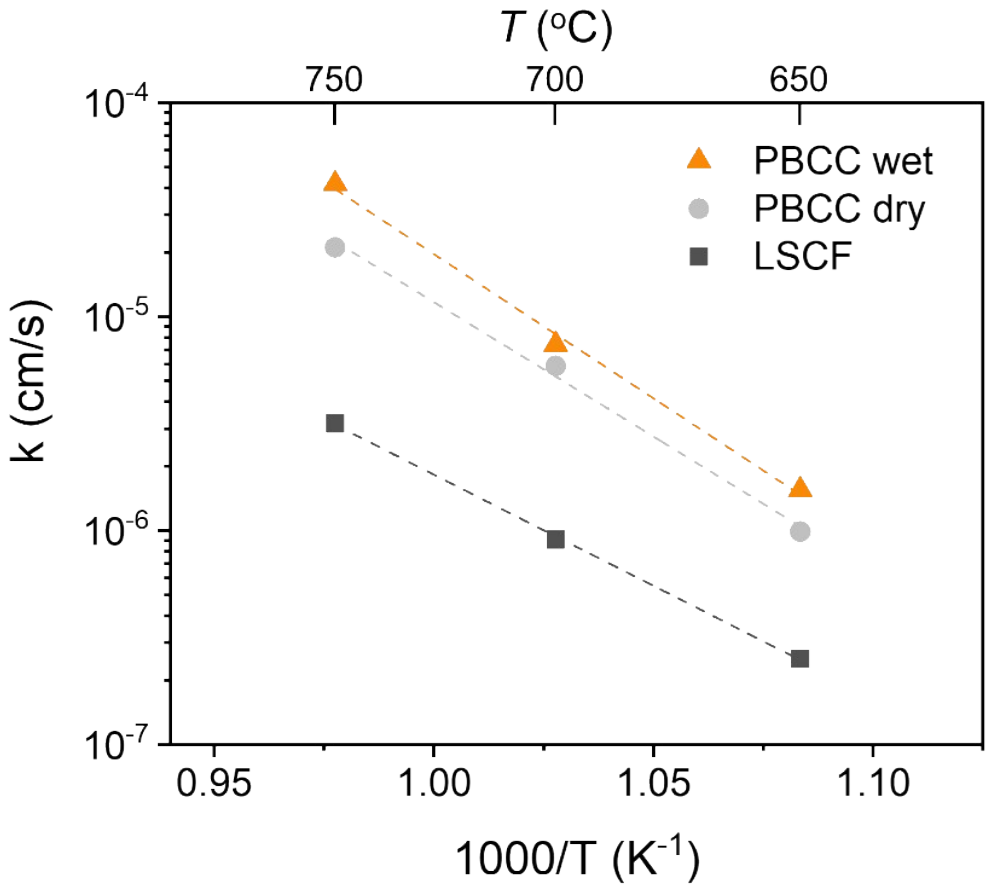

Figure S8. surface exchange co-efficient (k) values of wet-annealed PBCC (PBCC wet), pristine PBCC (PBCC dry) and LSCF

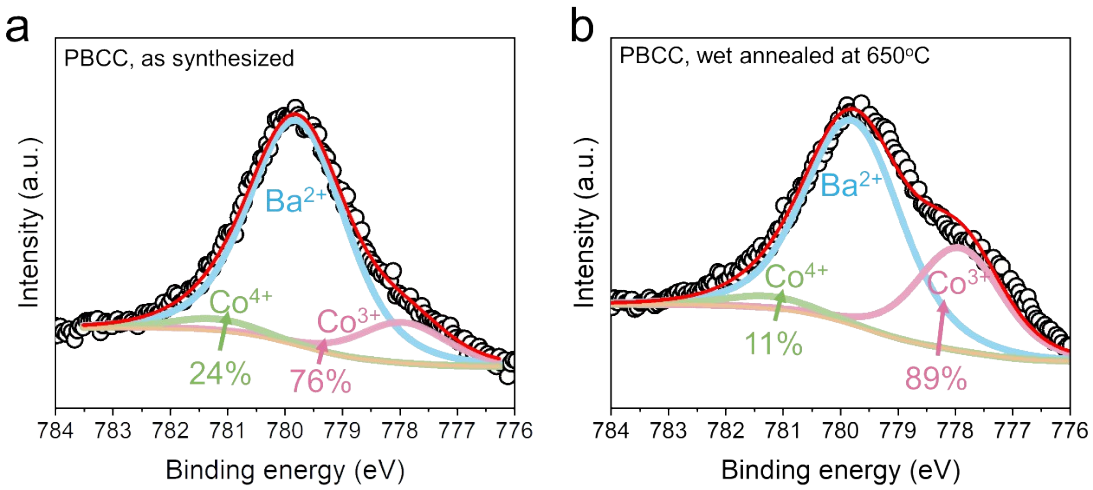

Figure S9. Co $2p_{3/2}$ and Ba $3d_{5/2}$ X-ray photoelectron spectra of the (a) as-synthesized PBCC and (b) wet-annealed PBCC (650°C, 3vol% H_2O/air).

The oxidation states of the cobalt ion are analyzed with XPS. Due to the direct overlap between Co $2p_{3/2}$ and Ba $3d_{5/2}$, the peaks were fitted together. The binding energies of Ba^{2+} is ~780 ± 0.3 eV, while the Co^{4+} and Co^{3+} are 781.5 ± 0.3 eV and 778.5 eV ± 0.3 eV, respectively.[14, 15] As a result, for as-synthesized PBCC sample, the concentrations of Co^{4+} and Co^{3+} are 24 and 76%, respectively. On the other hand, after wet exposure, the concentrations are changed to 11 and 89%, leading to a much higher ratio of Co^{3+}/Co^{4+}. The higher concentration of Co^{3+} is an indication of lower average valence of the B-site in multi-phase PBCC, implying the formation of BCO with high oxygen vacancy concentrations.[16, 17]

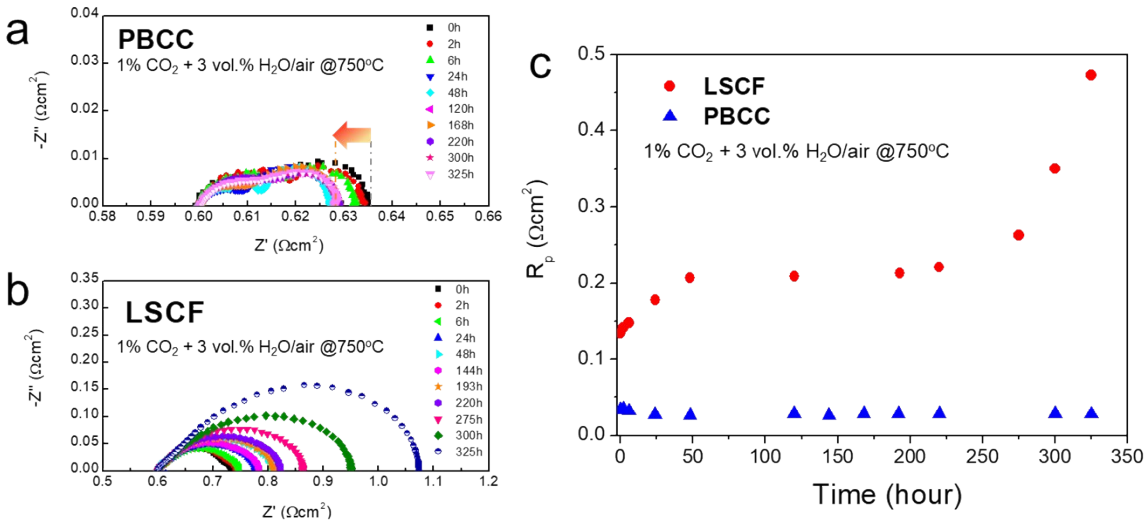

Figure S10. (a) Electrochemical impedance spectroscopy (EIS) spectra of PBCC (top) and LSCF (bottom) electrodes tested in 1% CO_2 + 3 vol.% H_2O/air at 750°C. (b) Long-term stability of PBCC electrodes in wet air compared to LSCF electrodes at 750°C.

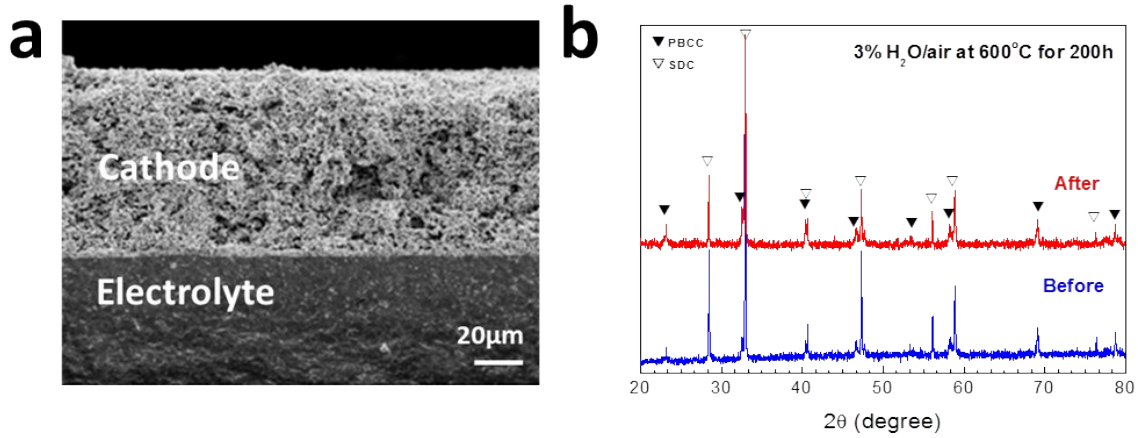

Figure S11. (a) SEM image of cross-sectional view of PBCC/SDC cell (b) XRD of PBCC/SDC/PBCC cell tested with 3 vol.% H_2O for 200 hours.

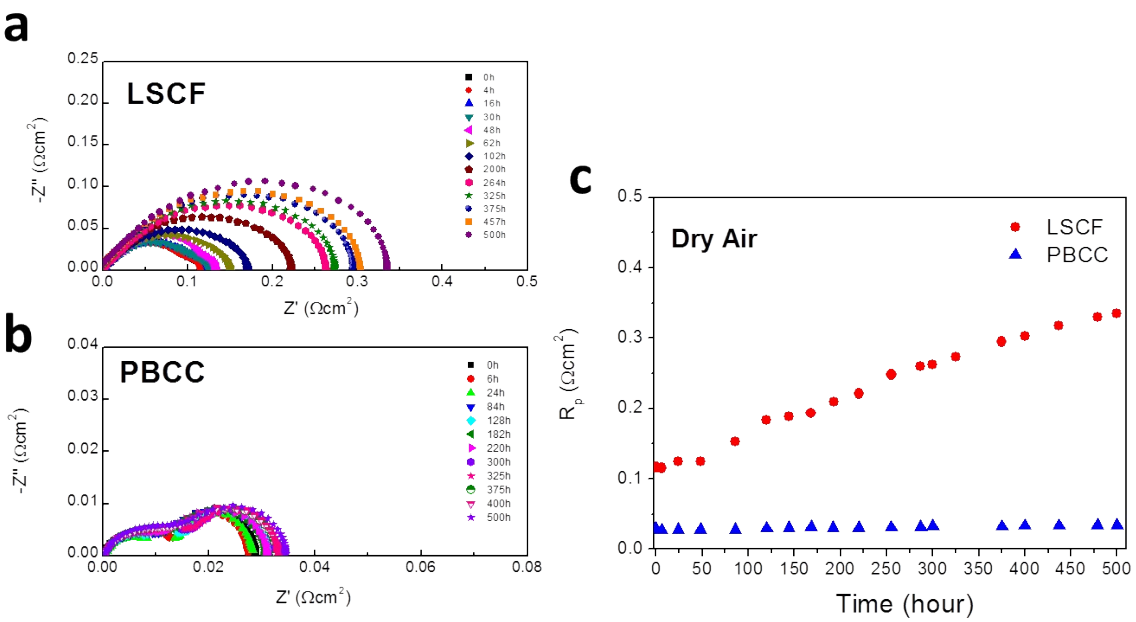

Figure S12. (a) Electrochemical impedance spectroscopy (EIS) spectra of LSCF/SDC/LSCF in

dry air at 750 °C (b) EIS spectra of PBCC/SDC/PBCC in dry air at 750 °C (c) Long-term stability of PBCC electrode in dry air compared with LSCF electrode at 750 °C.

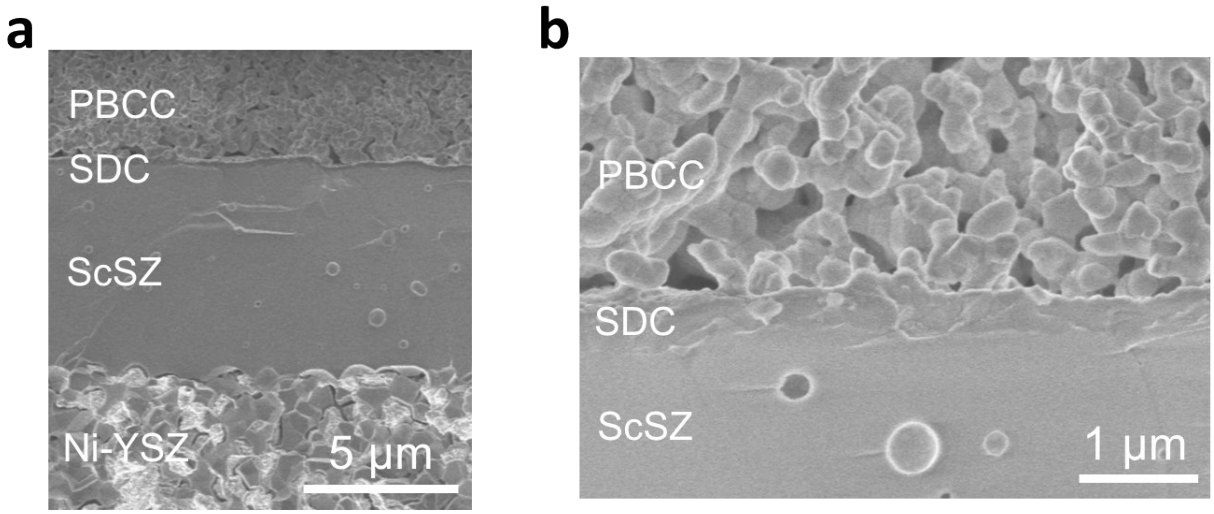

Figure S13. Cross-sectional SEM images of a button cell with configuration of (a) Ni-YSZ|ScSZ|SDC|PBCC and (b) magnified image of SDC buffer layer.

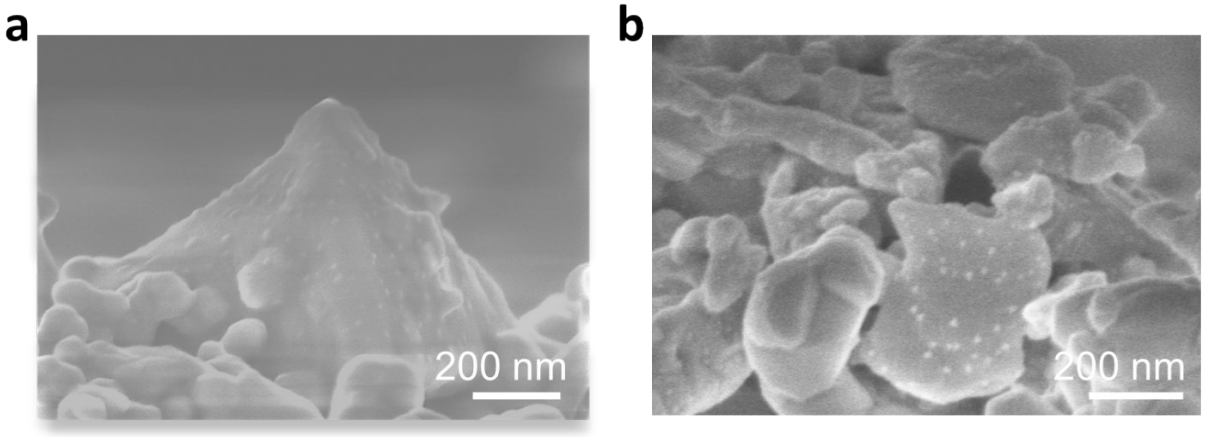

Figure S14. SEM images of a PBCC electrode after button cell operation with wet air oxidant.

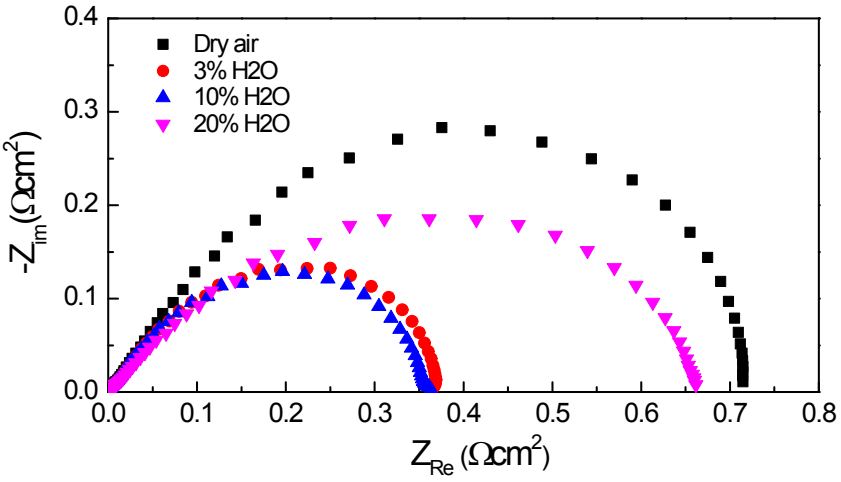

Figure S15. EIS spectra of a PBCC|SDC|PBCC symmetric cell testing in different water content air (dry, 3 vol.%, 10 vol.%, and 20 vol.% H_2O) at 600°C.

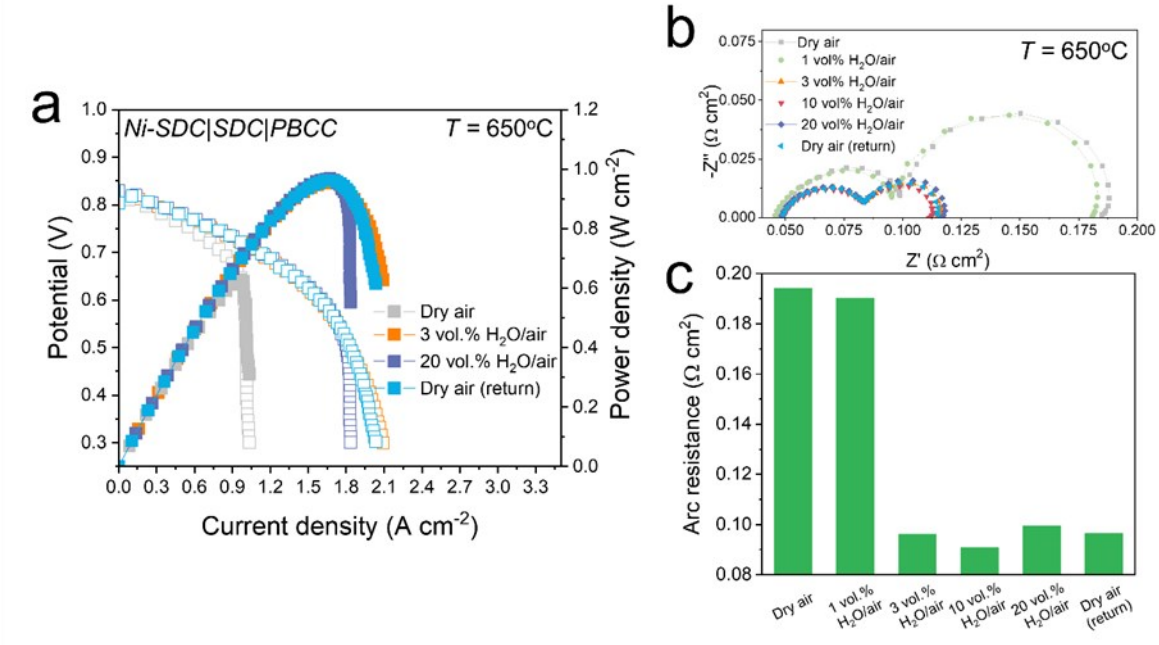

Figure S16. Electrochemical performance demonstration with button cells with a configuration of Ni-SDC|SDC|PBCC (Ni-SDC cell #1). Measurements were conducted in a following sequence: dry air→ 1 vol.% H_2O/air→ 3 vol.% H_2O/air→ 10 vol.% H_2O/air→ 20 vol.% H_2O/air→ dry air (return) (a) Typical polarization curves of a button cell with PBCC cathode at 650°C with varying oxidant as control variable. (b) Impedance spectra of single cell with various oxidants. (c) Comparison of the arc resistance under different oxidants.

We have characterized the performance of single cells based on PBCC cathode exposed to air with different humidity (Figure S14). Initially, the electrochemical performance of typical I-V, I-P curves and impedance spectra were measured in dry air. Without the water-mediated surface self-assembly, the peak power density of ~0.63 W cm^{-2} was achieved at 650°C. Initially, polarization resistance was ~0.194 Ω cm^2. (Measured arc resistances are corrected to find actual interfacial polarization resistance, which can be calculated by previously reported equation.[18]

$$R_p = \frac{R_T - R_b}{\frac{V_{OC}}{E_N}\left[1 - \frac{R_b}{R_T}\left(1 - \frac{V_{OC}}{E_N}\right)\right]}$$, where, R_p as polarization resistance (Ω cm^2), R_T as total resistance (Ω cm^2), R_b as resistance of bulk electrolyte (Ω cm^2), V_{oc} as open circuit voltage (V), E_N is Nernst potential(V)).

Subsequently, the oxidant was changed to 1 vol.% H_2O/air, and a small enhancement was confirmed in EIS as the arc resistance was reduced to ~0.190 Ω cm^2. Clearly, the concentration of 1 vol.% H_2O was not enough to fully promote the water-mediated surface self-assembly.

Then, we introduced 3 vol.% H_2O/air to the PBCC cathode. The water concentration was controlled by using a temperature controlled water bubbler. 3 vol.% H_2O/air is flowed for 3 hours and the electrochemical performance was again measured. Accordingly, the peak power density increased to ~0.95 W cm^{-2} in 3 vol% H_2O/air, ~51% enhancement compared to the pristine cell measured in dry air. The performance is even superior to that of the fuel cell based on a commercial Ni-YSZ cell (Figure 3f), which showed ~0.49 W cm^{-2} at 650°C. The electrode polarization resistance of the single cell was ~0.096 Ω cm^2 under 3 vol.% H_2O/air.

Subsequently, we further introduced higher level of humidity (10, 20 vol.% H_2O) into the air. The arc resistance at various oxidants are plotted in Figure S14c for visual comparison. In 10 vol% H_2O/air, it seemed the arc resistance is further decreased (~0.0909 Ω cm^2) rather than 3 vol.% H_2O/air, however 20 vol.% showed higher arc resistance (~0.0994 Ω cm^2) and we blame the diluted O_2 concentration in oxidants as confirmed in I-V curves.

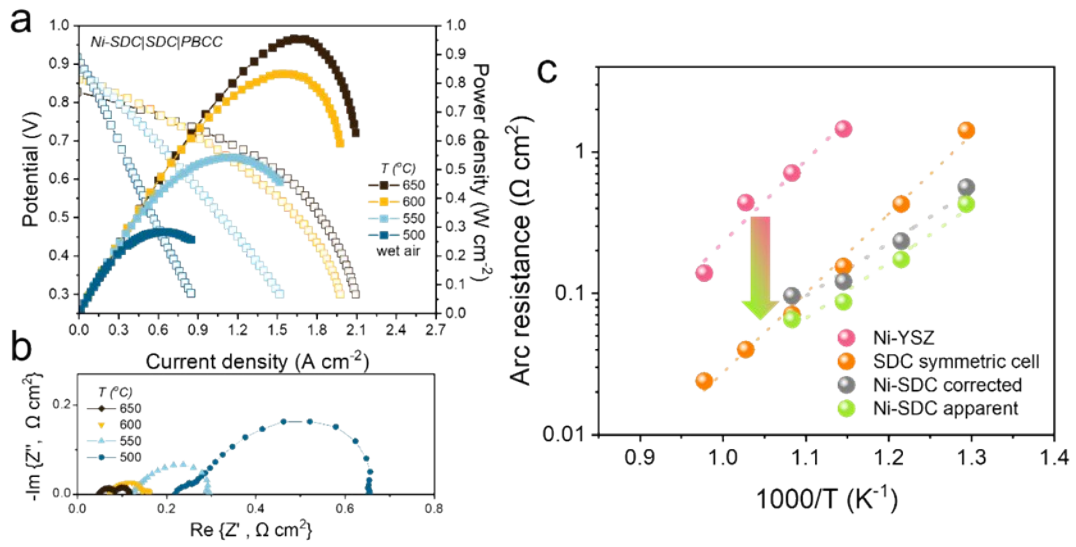

Figure S17. (a) Typical I-V, I-P curves measured at 500~650°C with continuous wet-air supply as oxidant. (b) According impedance spectra measured under open circuit voltage. (c) Comparison of the arc resistance measured in different configuration of cells using PBCC cathodes.

Since the interfacial resistances determined from the Ni-SDC|SDC|PBCC cells, or any mixed-conducting electrolyte based cells, are the 'apparent' resistances, not the 'actual' resistances because of the partial electronic conduction of the ceria electrolyte (such as SDC or GDC), as implied by the relatively low OCV (about 0.8V), the R_p is corrected to find actual interfacial polarization resistance, which can be calculated by previously reported equation.[18]

$$R_p = \frac{R_T - R_b}{\frac{V_{OC}}{E_N}\left[1 - \frac{R_b}{R_T}\left(1 - \frac{V_{OC}}{E_N}\right)\right]}$$

where, R_p as polarization resistance (Ω cm^2), R_T as total resistance (Ω cm^2), R_b as resistance of bulk electrolyte (Ω cm^2), V_{oc} as open circuit voltage (V), E_N is Nernst potential(V).

Accordingly, the R_p values can be calculated as in the Table S1.

Table S2. Electrochemical characteristics of Ni-SDC|SDC|PBCC cell under open circuit conditions.

T(°C)	R_T	R_b	V_{oc}	E_N	R_p
650	0.11418	0.04869	0.81224	1.07	0.09615
600	0.16082	0.0738	0.85599	1.08	0.121391
550	0.29511	0.12176	0.8857	1.1	0.234111
500	0.65073	0.22332	0.90168	1.11	0.562378

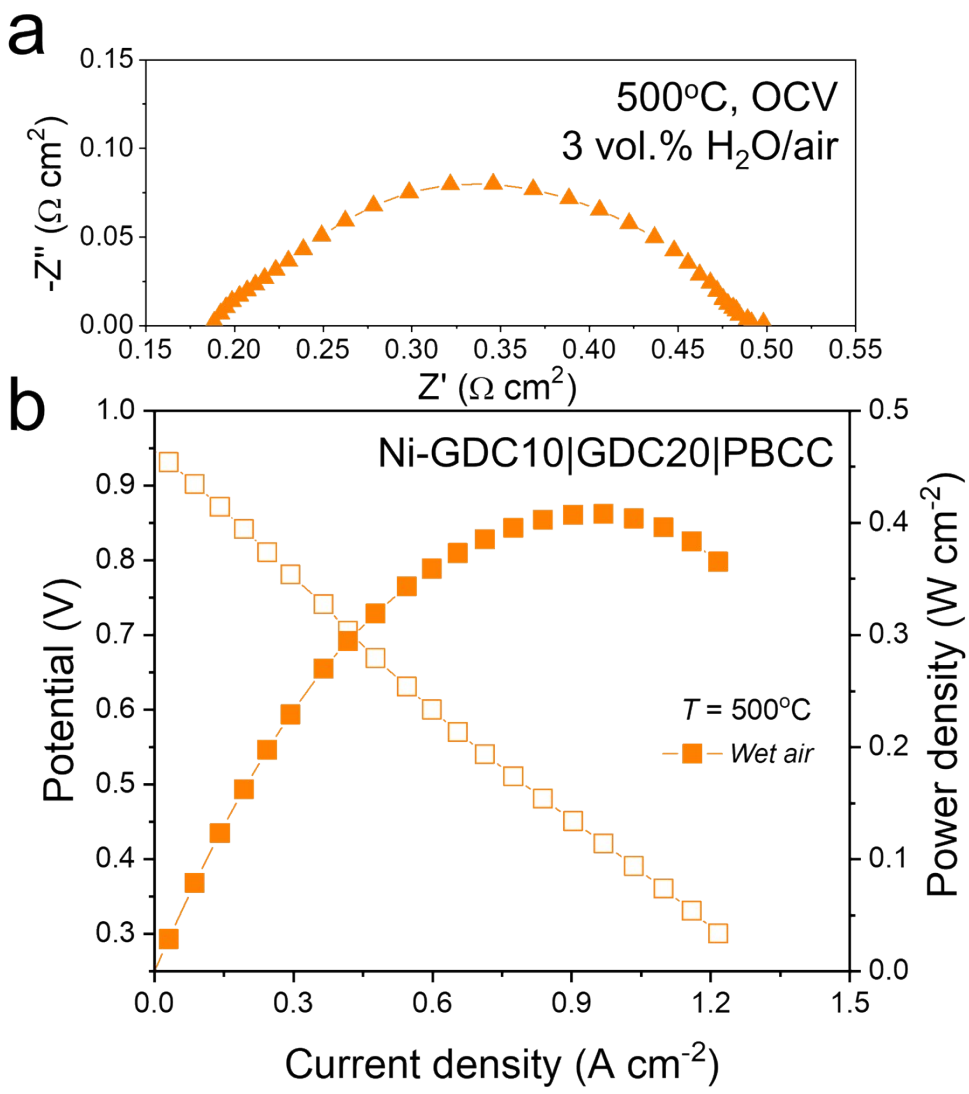

Figure S18. (a) Impedance spectra measured under open circuit voltage at 500°C with Ni-GDC10|GDC20|PBCC cell. 3 vol.% H_2O/air was fed to the cathode. (b) I-V characterization results of corresponding cell at 500°C.

Table S3. Performance comparison for SOFCs based on double-perovskites

Cell composition	Temperature (°C)	Peak power density (W cm^{-2})	Ref.
Ni-YSZ|ScSZ|SDC|water-mediated surface self-assembled PBCC	750	1.46	This work
Ni-SDC|SDC|water-mediated surface self-assembled PBCC	650	0.95	This work
Ni-GDC10|GDC20|water-mediated surface self-assembled PBCC	500	0.408	This work
Ni-BZCYYb|SDC|PrO_x infiltrated electrospun-$PrBa_{0.5}Sr_{0.5}Co_{1.5}Fe_{0.5}O_{5+\delta}$	500	0.43	[1]
Ni-BZCYYb|SDC|PBCC	650	0.72	[2]
Ni-YSZ|YSZ|SDC|BaO-coated PBCC	750	1.15	[3]
Ni-GDC|LDC|LSGM|$SmBaCo_2O_{5+\delta}$ -SDC	750	0.592	[4]
Ni-GDC|LDC|LSCM|$SmBaCo_{0.5}Mn_{1.5}O_{5+\delta}$	650	0.279	[5]
Ni-GDC|GDC|$Pr_{0.94}BaCo_2O_{5+\delta}$	500	0.21	[6]
Ni-SDC|SDC|LSGM|$YBaCo_2O_{5+\delta}$	750	0.361	[7]
Ni-SDC|SDC|$LaBa_{0.5}Sr_{0.25}Ca_{0.25}Co_2O_{5+\delta}$	800	0.662	[8]

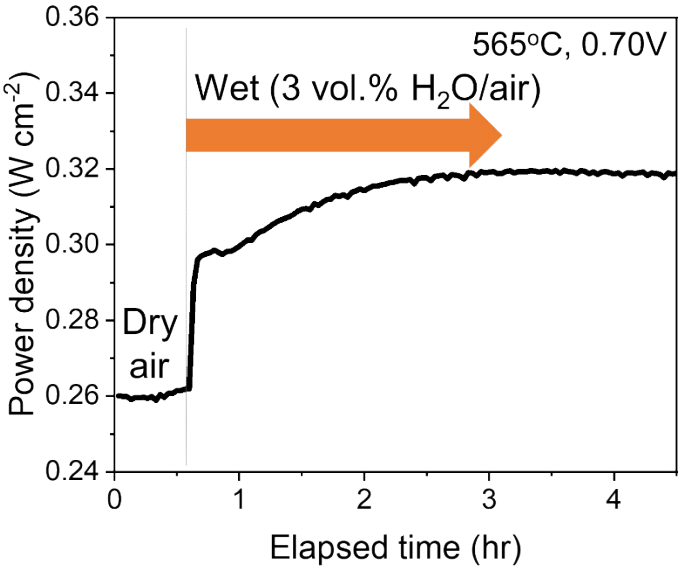

Figure S19. Change in power density of the PBCC based button cell (cell #2, Ni-SDC|SDC|PBCC) as the oxidant was switched from dry air to wet air containing 3% water vapor. (0.70V at 565°C)

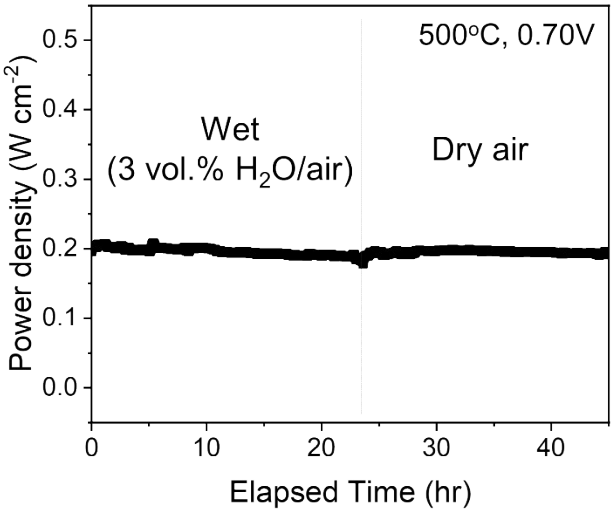

Figure S20. Change in power density of the PBCC based button cell (cell #2, Ni-SDC|SDC|PBCC), after the cathode experienced water-mediated surface self-assembly (as described in Figure R11), as the oxidant was switched from wet air to dry air.

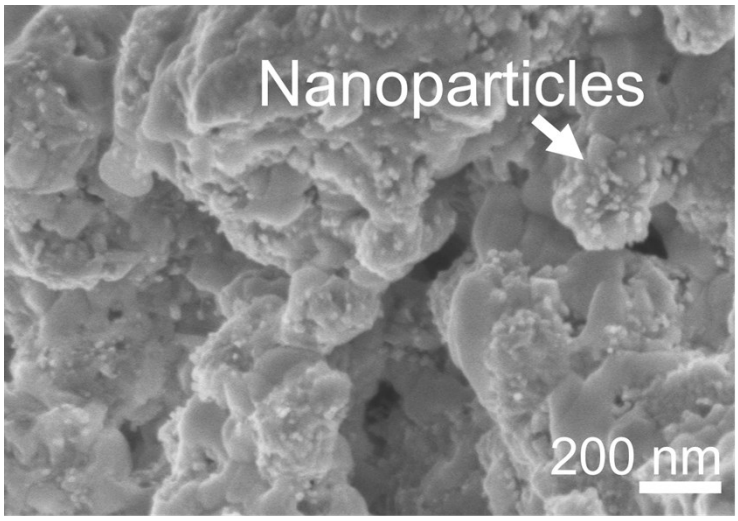

Figure S21. The surface morphology of PBCC cathode (Ni-SDC cell #2) after the testing as described in Figure S19-S20.

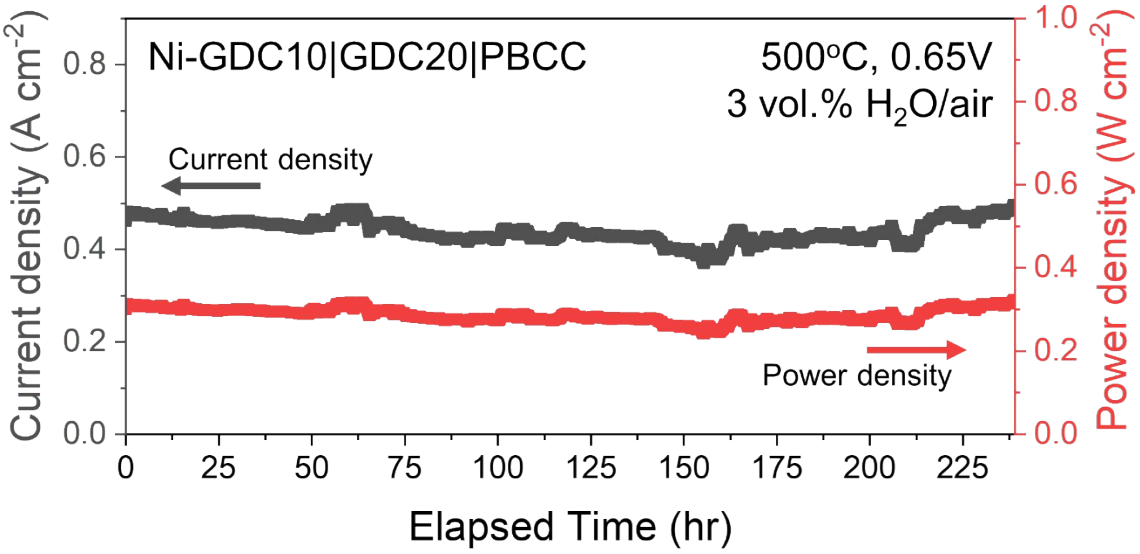

Figure S22. Temporal evolution of current density and power density under constant voltage load of 0.65V. 3 vol.% H_2O/air was constantly supplied to the cathode.

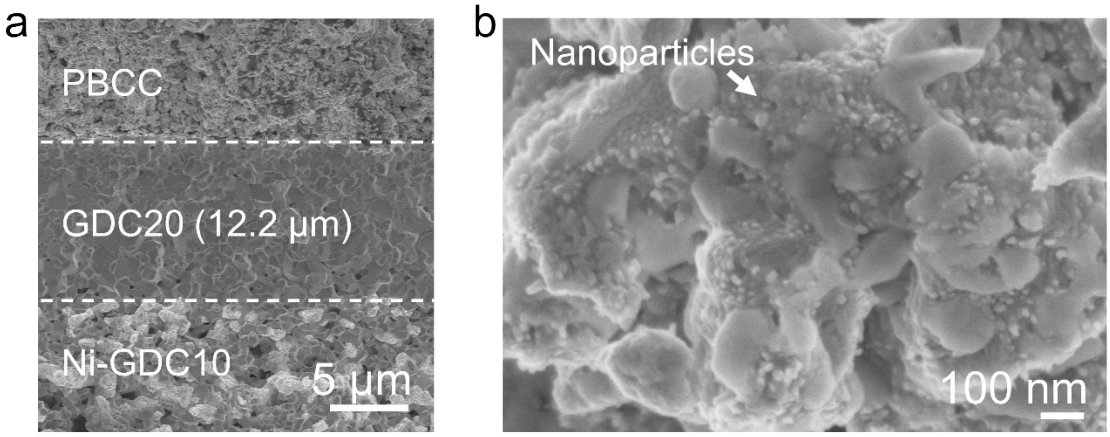

Figure S23. (a) Cross-sectional SEM image of Ni-GDC10|GDC20|PBCC single cell after long-term stability testing (at 500°C for 230 hours). (b) PBCC cathode microstructure after stability testing under wet air at 500°C for 230 hours.

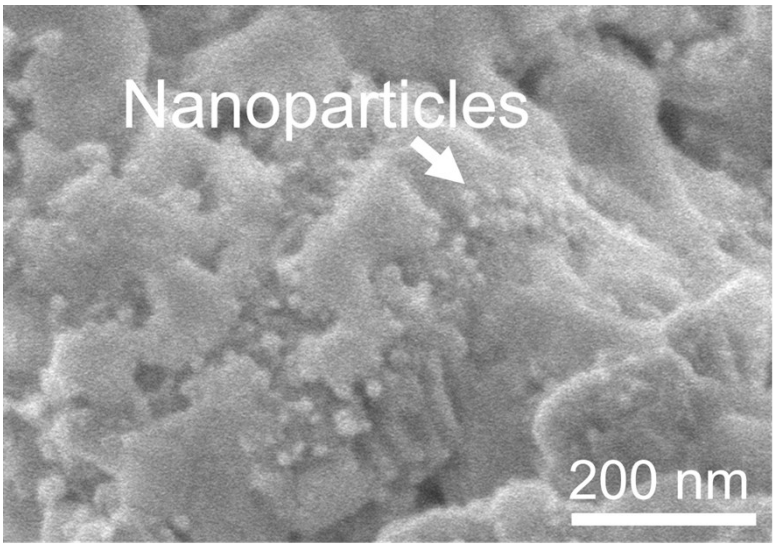

Figure S24. PBCC cathode microstructure after stability testing (at 500^{o}C for 230 hours) in wet air. In situ grown nanoparticles are observable throughout the cathode.

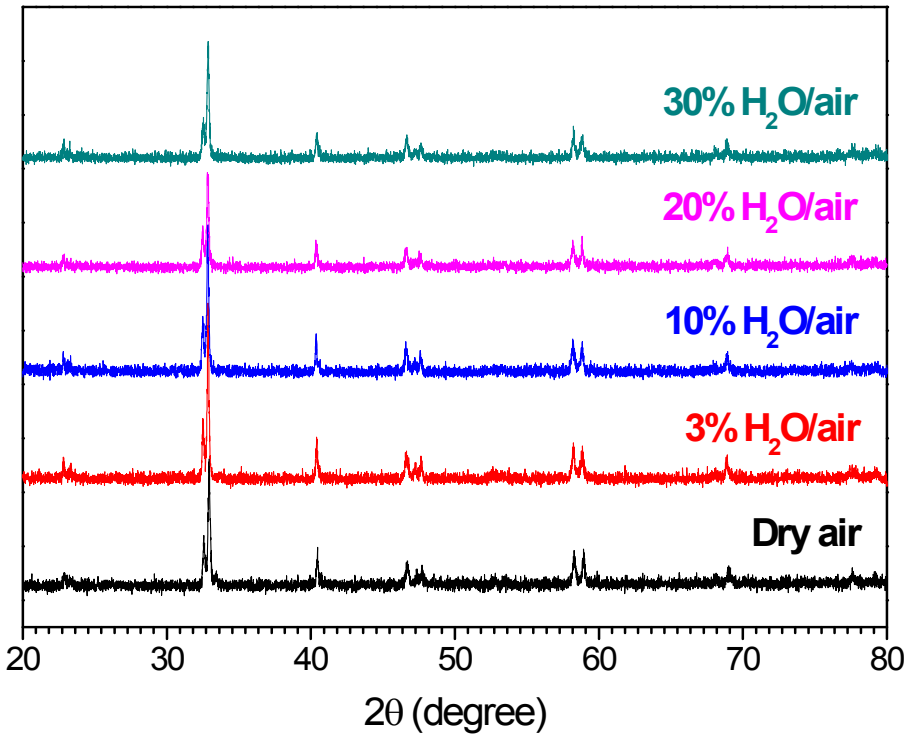

Figure S25. Typical XRD data of PBCC powder exposed to different water vapor pressure.

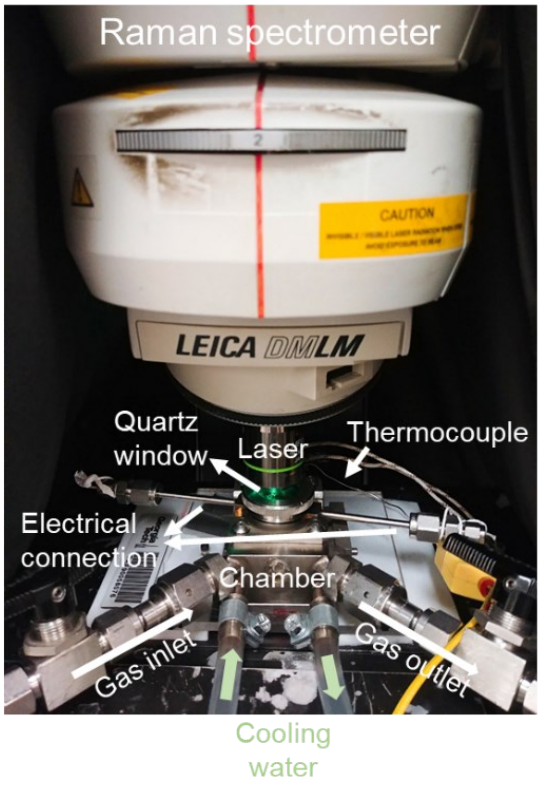

Figure S26. Experimental set-up for *in situ* Raman spectroscopy. The gas- and temperature-controllable Raman chamber was purchased from Harrick Science (with some modifications for electrical connection).

To perform in situ Raman spectroscopy study, the electrode to be characterized was faced up for direct exposure to laser excitation. With a heating element under the sample holder inside the chamber, which is surrounded by cooling water, the temperature of the platform can be varied from room temperature to ~600^{0}C. Moreover, the chamber can have controlled atmosphere by flowing an inlet gas with a mass flow controller. Thus, the use of this platform enables us to track the evolution of key spectroscopic features of PBCC electrodes exposed to various gas mixtures with different humidity, allowing us to record changes in the position, profile, and intensity of Raman band as experimental conditions are systematically changed.

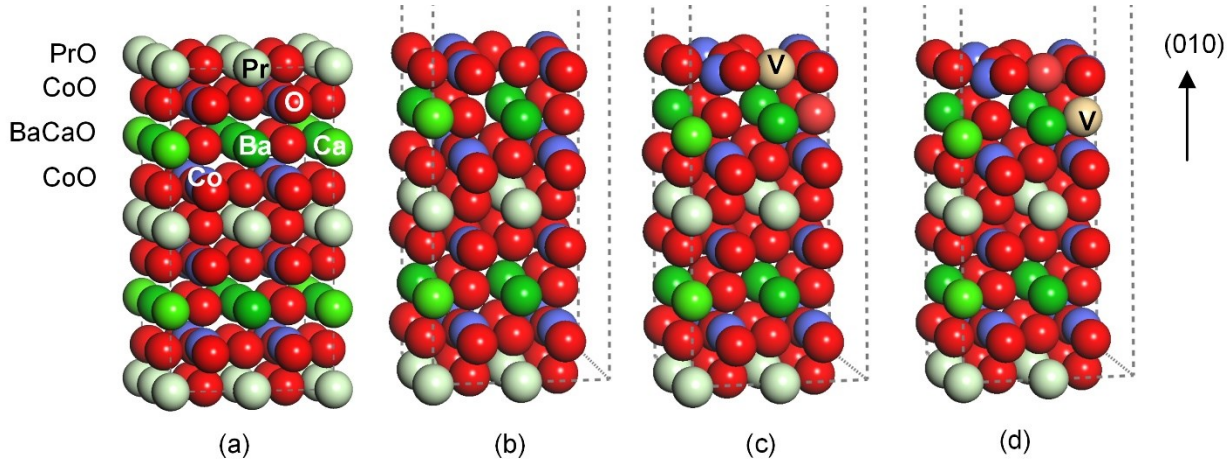

Figure S27. (a) The bulk structure of PBCC ($PrBa_{0.75}Ca_{0.25}CoO_{6.0}$) ($Pr_4Ba_3Ca_1Co_8O_{24}$; *P4/mmm*) optimized at GGA-PBE. PBCC is a double-layered structure. a=b=3.8767Å and c=7.5667Å. (b) A perfect 8-atomic-layer PBCC(010) surface. (c) A defective surface model with one oxygen vacancy on the topmost surface. (d) A defective surface model with one oxygen vacancy in the first sub-lattice. A vacuum of 15Å is used, and the models are CoO-terminated. "**V**" corresponds to an oxygen vacancy.

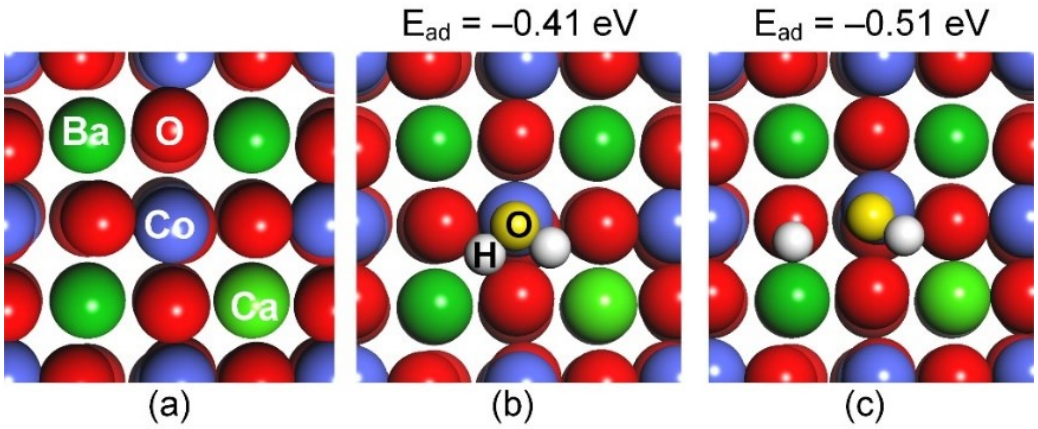

Figure S28. Top views of (a) a perfect PBCC(010) surface, (b) adsorbed H_2O on a Co ion, and (c) dissociated H_2O. From a transition-search calculation, it was confirmed that the dissociation of HOH occurs without a barrier.

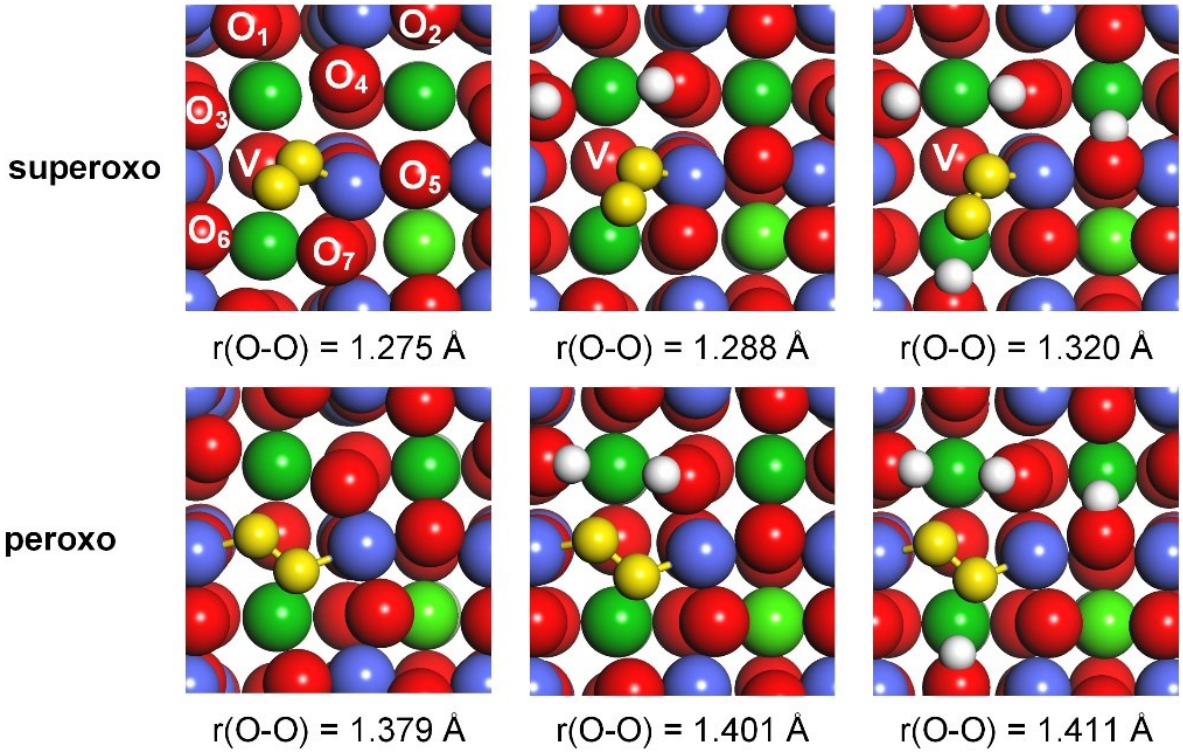

Figure S29. Top views of adsorbed surface species on a defective PBCC(010) surface with an oxygen vacancy. O_1, O_2, O_3, O_4, O_5, O_6, and O_7 are the seven active sites forming hydroxyl species. The configurations are representative for 0, 2/7, and 3/7 monolayers, respectively. The O-O bond length increases as the concentration of hydroxyl species increases, resulting in the higher attraction between oxygen and hydrogen moieties. This effect also influences the reaction barrier height of the concurrent dissociation and diffusion into the sub-lattice of peroxo species as discussed in the text.

Table S4. Summary of calculated vibrational frequencies[a] for a "superoxo" species as a function of surface hydroxyl species.

	Condition													
	dry		wet											
No. OH	0		1		2		3		4		5		6	
	freq	mode	freq	mode	freq	mode	freq	mode	freq	mode	freq	mode	freq	mode
1	1257	**os**	3723	**hs**	3713	**hs**	3720	**hs**	3685	**hs**	3726	**hs**	3684	**hs**
2			1247	**os**	3701	**hs**	3711	**hs**	3668	**hs**	3675	**hs**	3670	**hs**
3					1239	**os**	3364	**hs**	3634	**hs**	3660	**hs**	3664	**hs**
4							1141	**os**	3321	**hs**	3654	**hs**	3656	**hs**
5									1134	**os**	3180	**hs**	3565	**hs**
6									941	**ht**	1113	**os**	2619	**hs**
7									910	**ht**	1015	**ht**	1369	**ht +os**
8									827	**ht**	858	**ht**	1012	**os**
9									795	**ht**	853	**ht**	917	**ht +os**
10											816	**ht**	885	**ht +os**
11											769	**ht**	855	**ht**
12													822	**ht**
13													778	**ht**

[a] For the assignment, "**os**", "**hs**", and "**ht**" are the O-O stretching, the $O_{surface}$-H stretching, and the $O_{surface}$-H twisting modes, respectively. "**ht + os**" represents the mixed stretching mode of $O_{surface}$-H twisting and O-O. Using the O-O vibrational frequencies in red in Table S1 and S2, the correlation curves was prepared as shown in the text.

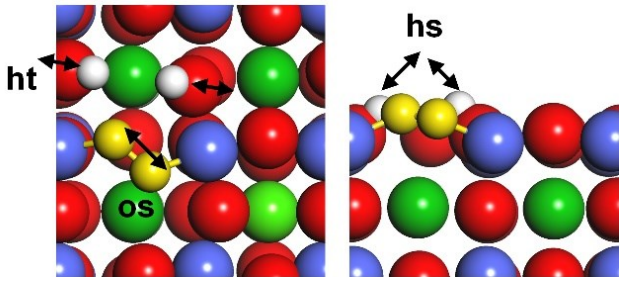
ht
os
hs

Table S5. Summary of calculated vibrational frequencies for a "peroxo" species as a function of surface hydroxyl species.

	Condition									
	dry		wet							
No. OH	0		2[a]		3		5		7	
	freq	mode	freq	mode	freq	mode	freq	mode	freq	mode
1	917	**os**	3711	**hs**	3727	**hs**	3698	**hs**	3732	**hs**
2			3593	**hs**	3704	**hs**	3674	**hs**	3712	**hs**
3			1061	**os**	3507	**hs**	3672	**hs**	3697	**hs**
4			891	**oo**	915	**os**	3621	**hs**	3661	**hs**
5			841	**os + ht**	898	**os + ht**	3465	**ht**	3541	**hs**
6					803	**os + ht**	965	**hs**	3531	**hs**
7							878	**os**	3408	**hs**
8							840	**ht**	1013	**ht**
9							819	**os+ht**	934	**ht**
10							778	**ht**	857	**os**

[a] For the correlation between vibrational frequencies and the surface coverage shown in the text, 910 cm^{-1} was used after averaging with another O-O stretching mode of 929 cm^{-1} at 2/7ML.

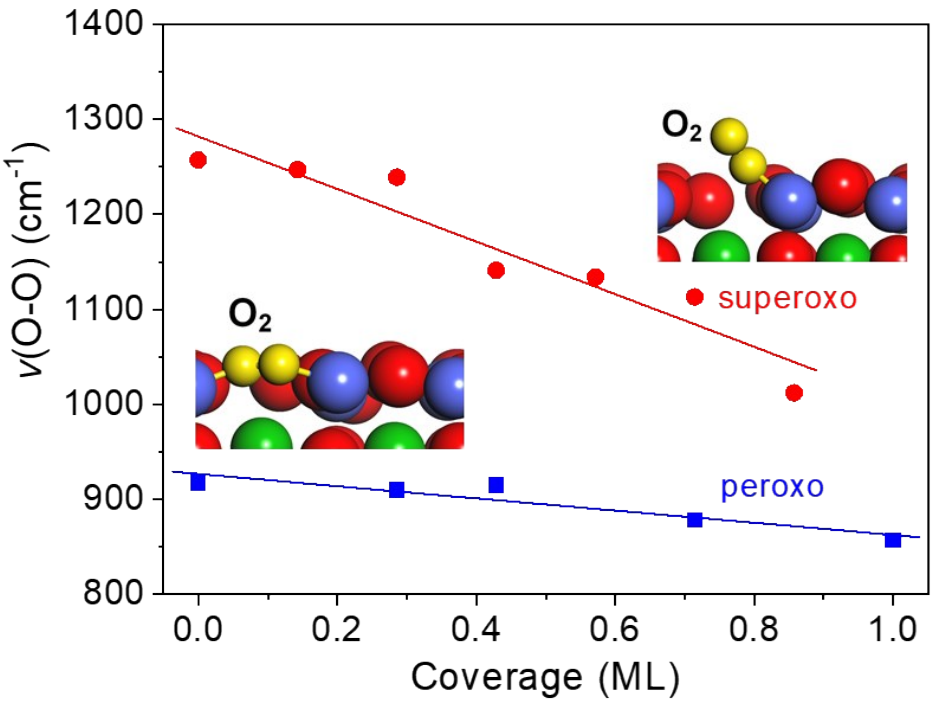

Figure S30. Correlation of calculated vibrational frequencies of the O-O stretching mode for superoxo and peroxo species with and without water as a function of surface hydroxyl species. "0" ML refers to a dry condition.

This correlation reveals that the hydroxyl species that formed on PBCC via water dissociation strongly attracts the O-O moiety, resulting in its elongation as the concentration of the hydroxyl species increases (for the superoxo species the range was from 1.27 Å to 1.29 Å and for the peroxo species the range was from 1.38 Å to 1.40 Å). We examined the change of the oxygen species at 0 and 1ML of hydroxyl species by means of a Bader charge analysis,[19] leading to an increase in the charge upon the addition of water (*i.e.*, superoxo species from –0.35*e* to –1.05*e* and peroxo species from –1.22*e* to –2.18*e*).

Supplementary References

1. M. Saccoccio, T. H. Wan, C. Chen and F. Ciucci, *Electrochim. Acta*, 2014, **147**, 470-482.
2. T. H. Wan, M. Saccoccio, C. Chen and F. Ciucci, *Electrochim. Acta*, 2015, **184**, 483-499.
3. F. Ciucci and C. Chen, *Electrochim. Acta*, 2015, **167**, 439-454.
4. Y. Chen, S. Yoo, W. Zhang, J. H. Kim, Y. Zhou, K. Pei, N. Kane, B. Zhao, R. Murphy and Y. Choi, *ACS catal.*, 2019.
5. K. S. Blinn, H. Abernathy, X. Li, M. Liu, L. A. Bottomley and M. Liu, *Energy Environ. Sci.*, 2012, **5**, 7913-7917.
6. G. Kresse and J. Furthmuller, *Phys. Rev. B*, 1996, **54**, 11169-11186.
7. P. E. Blöchl, *Phys. Rev. B*, 1994, **50**, 17953-17979.
8. Y. Chen, Y. Choi, S. Yoo, Y. Ding, R. Yan, K. Pei, C. Qu, L. Zhang, I. Chang, B. Zhao, Y. Zhang, H. Chen, Y. Chen, C. Yang, B. deGlee, R. Murphy, J. Liu and M. Liu, *Joule*, 2018, **2**, 938-949.
9. Y. Chen, S. Yoo, Y. Choi, J. H. Kim, Y. Ding, K. Pei, R. Murphy, Y. Zhang, B. Zhao, W. Zhang, H. Chen, Y. Chen, W. Yuan, C. Yang and M. Liu, *Energy Environ. Sci.*, 2018, **11**, 2458-2466.
10. J. P. Perdew, K. Burke and M. Ernzerhof, *Phys. Rev. Lett.*, 1996, **77**, 3865-3868.
11. Y. A. Mastrikov, M. M. Kuklja, E. A. Kotomin and J. Maier, *Energy & Environ. Sci.*, 2010, **3**, 1544-1550.
12. H. J. Monkhorst and J. D. Pack, *Phys. Rev. B*, 1976, **13**, 5188-5192.
13. G. Henkelman, B. P. Uberuaga and H. Jónsson, *J. Chem. Phys.*, 2000, **113**, 9901-9904.
14. X. Kuai, G. Yang, Y. Chen, H. Sun, J. Dai, Y. Song, R. Ran, W. Wang, W. Zhou and Z. Shao, *Advanced Energy Materials*, 2019, **9**, 1902384.
15. X. Cui, R. O'Hayre, S. Pylypenko, L. Zhang, L. Zeng, X. Zhang, Z. Hua, H. Chen and J. Shi, *Dalton Transactions*, 2017, **46**, 13903-13911.
16. Y. Chen, Y. Choi, S. Yoo, Y. Ding, R. Yan, K. Pei, C. Qu, L. Zhang, I. Chang and B. Zhao, *Joule*, 2018.
17. Y. Chen, S. Yoo, W. Zhang, J. H. Kim, Y. Zhou, K. Pei, N. Kane, B. Zhao, R. Murphy, Y. Choi and M. Liu, *ACS catal.*, 2019, DOI: 10.1021/acscatal.9b01738, 7137-7142.
18. M. Liu and H. Hu, *J. Electrochem. Soc.*, 1996, **143**, L109.
19. G. Henkelman, A. Arnaldsson and H. Jónsson, *Computational Materials Science*, 2006, **36**, 354-360.